Efficient orbital torque in polycrystalline ferromagnetic-metal/Ru/Al_2O_3 stacks: Theory and experiment

Liyang Liao,[1,*] Fenghua Xue,[2,*] Lei Han,[3] Junyeon Kim,[4] Ruiqi Zhang,[3] Lun Li,[2] Jiuming Liu,[2] Xufeng Kou,[2,†] Cheng Song,[3,†] Feng Pan,[3] and YoshiChika Otani[1,4,†]

[1]*Institute for Solid State Physics, University of Tokyo, Kashiwa 277-8581, Japan*

[2]*School of Information Science and Technology, ShanghaiTech University, Shanghai 201210, China*

[3]*Key Laboratory of Advanced Materials (MOE), School of Materials Science and Engineering, Tsinghua University, Beijing 100084, China*

[4]*Center for Emergent Matter Science, RIKEN, Wako, Saitama 351-0198, Japan*

(Received 23 November 2021; revised 14 March 2022; accepted 14 March 2022; published 30 March 2022)

Recently emergent current-induced orbital torque is considered more effective for magnetization switching than the well-established spin-orbit torque. However, long-range orbital transport in polycrystalline films and the theory on orbital transport in polycrystalline heterostructures remain elusive. Here we report a large torque effect in CoFeB/Ru/Al_2O_3 polycrystalline stacks. The unfilled d-shell and small spin-orbit coupling in Ru provide an ideal platform for orbital generation and transport. The orbital current from the Ru/Al_2O_3 interface can go through a thick Ru layer, with a peak value at 7-nm-thick Ru, and then induces a strong torque effect in CoFeB. The torque efficiency increases unprecedentedly with increasing CoFeB layer thickness, leveling off at $\sim$0.3 for 12-nm-thick CoFeB. Theoretical analysis shows that the orbital transport in polycrystalline materials exhibits a unique random precession behavior, leading to a more efficient orbital transport than that in single crystals. Besides the fundamental significance, our findings advance the development of practical orbital torque devices.

DOI: 10.1103/PhysRevB.105.104434

I. INTRODUCTION

The efficient current-induced spin-torque effect is of great significance for developing spintronic memory and logic devices. In the past decade, there has been intensive focus on spin-orbit torque, which utilizes spin-orbit coupling (SOC) in heavy metals (and/or Rashba interfaces) to generate spin current and resultant torque to manipulate the magnetization of an adjacent ferromagnetic layer [1–3]. Recently, great interest has emerged on the torque effect based on orbital angular momentum injection and SOC in the ferromagnet called orbital torque (OT) [4–8]. While spin current carries, at most, $\hbar/2$ angular momentum with each electronic state, the angular momentum carried with a state in an orbital current has no limitation, suggesting a more significant efficiency with OT. Indeed, theoretically, orbital-current generation efficiency is much larger than its spin counterpart in most metal elements [7,9]. Also, materials selection for the orbital source is extremely wide due to SOC not being necessary, instead of being limited to a few kinds of heavy metals like spin-current generation [10]. These make OT an attractive candidate for the operation principle of practical spintronic devices.

Industrial on-silicon production requires the development of OT devices based on polycrystalline stacks. In previous reports, OT was experimentally observed in polycrystalline stacks prepared by room-temperature evaporation or sputtering [4–6,11–13], mainly based on the interfacial orbital Rashba effect (ORE), with the possibility of controlling OT by layer design [4–6,12]. In these reports, an interface or a bulk containing Cu or Pt is utilized as a source of orbital angular momentum. However, the filled d-shell of Cu [5] and the large SOC of Pt [6] hinder orbital transport and complicate the analysis of OT in polycrystalline stacks. It is also reported that orbital transport in Cu is assisted by oxidation, which surely would provide a complexity on the structure [14]. Meanwhile, due to the complexity of orbital transport in polycrystalline heterostructures, theoretical works have focused on orbital generation and transport in single crystalline structures [15,16]. It is highly warranted to bridge the gap between experiment and theory by obtaining efficient, long-range orbital transport in a uniform polycrystalline layer and developing a corresponding theory on orbital transport, which remains elusive.

In this work, we experimentally study the current-induced torque effect in polycrystalline ferromagnetic metal (FM)/Ru/Al_2O_3 stacks [Fig. 1(a)], and demonstrate a high torque efficiency due to the ORE at the Ru/Al_2O_3 interface. Ru is chosen because of its electronic configuration of $4d^7 5s^1$ and a small bulk-originating spin-orbit torque [17] so that orbital current generation is allowed by orbital hybridization, orbital current propagation is not limited by the absence of d-electrons at the Fermi level or SOC-related relaxation, and OT is not disturbed by the conventional spin Hall torque. We also propose a theoretical orbital generation and transport model across polycrystalline stacks, showing that orbital transport

*These authors contributed equally to this work.

†kouxf@shanghaitech.edu.cn; songcheng@mail.tsinghua.edu.cn; yotani@issp.u-tokyo.ac.jp

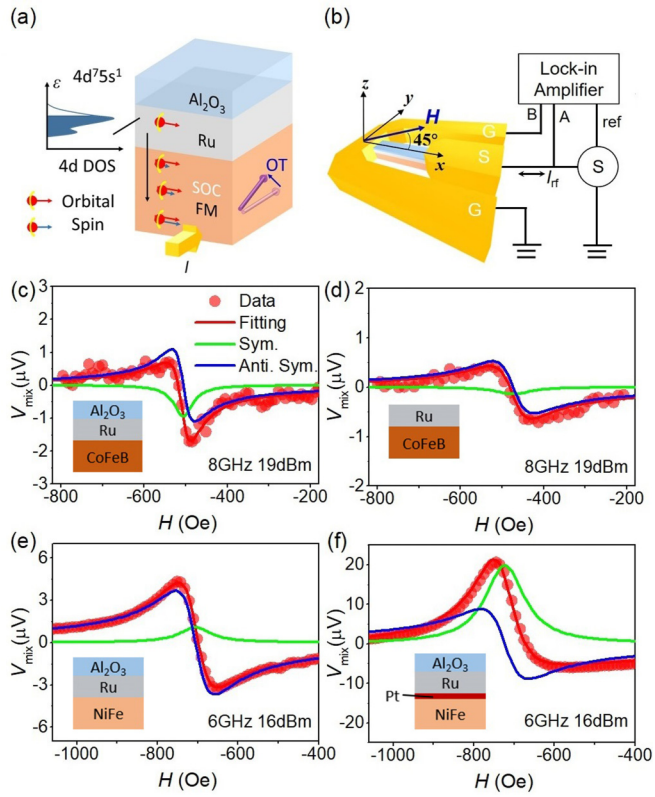

FIG. 1. (a) Schematic of the orbital torque in FM/Ru/Al_2O_3. (b) Experimental setup of the ST-FMR measurement. (c)–(f) ST-FMR spectra and fitting for the CoFeB(7)/Ru(6)/Al_2O_3(2) (c) and CoFeB(7)/Ru(6) (d) devices at 8 GHz, and NiFe(7)/Ru(6)/Al_2O_3(2) (e) and NiFe(7)/Pt(1)/Ru(6)/Al_2O_3(2) (f) devices at 6 GHz. The red circles are experimental data; the red lines are fitting curves. The symmetric and antisymmetric components are plotted in the right panel with green and blue lines, respectively. Schematics of the sample layout are shown in the inset.

can be even more efficient than that in single-crystal structures with perfect crystal fields.

II. EXPERIMENT

We performed spin-torque ferromagnetic resonance (ST-FMR) measurements [Fig. 1(b)] on polycrystalline FM/Ru/Al_2O_3 stacks prepared by room-temperature sputtering on thermally oxidized Si/SiO_2 substrate. In Fig. 1(c), we show the $V_{\rm mix}$ signal obtained from the ST-FMR measurement of a $Co_{40}Fe_{40}B_{20}$(7)/Ru(6)/Al_2O_3(2) stack (units in nanometers) trilayer. The current-induced torque drives magnetization precession at the resonance condition, giving rise to a resonance peak. The ST-FMR spectrum is fitted by the asymmetric (A) and symmetric (S) Lorentzian components. As shown in Fig. 1(a), a sizable negative S component is observed for the CoFeB(7)/Ru(6)/Al_2O_3(2) stack, demonstrating the existence of the current-induced damping-like torque. Note that the small amplitude of the resonance signal is due to the small in-plane magnetoresistance ($\sim 0.06\%$) of CoFeB, and the possible spin-pumping contribution to S is excluded [18]. The small signal cannot survive with large dc current injection, making it difficult to evaluate torque efficiency via current-induced damping modulation. We also note that the thick CoFeB layer and the large demagnetization field hinder a reliable signal from the second harmonic measurement technique. Hence, torque efficiency is mainly evaluated by analyzing ST-FMR spectra. Additionally, we also perform a unidirectional spin Hall magnetoresistance (USMR) measurement to provide additional independent evidence for the presence of the torque. The USMR could be sufficiently large due to the large spin polarization of CoFeB, as discussed later.

Utilizing the ST-FMR spectrum, we evaluate the current-induced torque efficiency $\xi_{\rm FMR}$ with the following equation [19,20]:

$$\frac{j_{\rm L}}{j_{\rm C}} \approx \xi_{\rm FMR} = \frac{S}{A}\frac{4\pi M_{\rm s} e t_{\rm F} t_{\rm Ru}}{\hbar}\left[1+\frac{4\pi M_{\rm eff}}{H_0}\right]^{1/2}, \qquad (1)$$

where $j_{\rm L}$ is the angular momentum current density absorbed by the FM layer, $j_{\rm C}$ is the charge current density in the Ru layer, $M_{\rm s}$ is the saturated magnetization, e is the elementary charge, $\hbar$ is the reduced Planck constant, $t_{\rm F}$ is the thickness of the FM layer, and $t_{\rm Ru}$ is the thickness of the Ru layer. We found that the sign of observed A is unchanged for all devices, consistent with the sign of the Oersted field torque [19]. It supports the restricted or negligible contribution of the field-like torque for the A component in the thick FM thickness regime [20]. For the CoFeB(7)/Ru(6)/Al_2O_3(2) stack, $\xi_{\rm FMR}$ is evaluated to -0.15, which is even larger than the spin-torque efficiency of the widely used heavy metal Pt ($\sim$0.1). In contrast, the S component becomes much smaller in CoFeB(7)/Ru(6) [Fig. 1(d)], corresponding to $\xi_{\rm FMR} = -0.04$, less than one-third of that in the sample with the Al_2O_3 capping. These contrasting values of $\xi_{\rm FMR}$ indicate that the generation of the orbital current dominantly comes from the Ru/Al_2O_3 interface rather than the CoFeB/Ru interface or the bulk Ru layer.

Interestingly, less than five times smaller $|\xi_{\rm FMR}| = 0.03$ is observed for $Ni_{80}Fe_{20}$/Ru(6)/Al_2O_3(2), where only the FM layer is replaced from CoFeB to $Ni_{80}Fe_{20}$ [Fig. 1(e)]. Such a large difference is difficult to explain by the different interfacial transparencies depending on the FMs [20,21]. Instead, it indicates that the generation mechanism of the large torque is deeply linked to the FM layer. On the contrary, we obtain large and positive S component, corresponding to $|\xi_{\rm FMR}| = 0.08$, after inserting a thin Pt layer (1 nm) between the NiFe and Ru layers [Fig. 1(f)]. The distinct torque efficiency dependent on the FM could originate from the different orbital-to-spin conversion efficiency $\eta_{\rm L-S}$, which is also related to the spin Hall effect (SHE) and the anomalous Hall effect (AHE). In the literature, we find that CoFeB has negative SHE [22]. Also, numbers of effect originated by SOC—for example, AHE and spin-rotation coupling in NiFe with a composition rate around Ni : Fe = 80 : 20 —are commonly very small, possibly deeply connected to the opposite sign of the AHE between polycrystalline Ni and Fe [23,24]. Therefore, an extra layer is required in order to obtain large torque when FM = NiFe, and it is realized after inserting the Pt layer, which has large and positive $\eta_{\rm L-S}$ [7,9]. Note that the opposite sign of OT is observed between Fe/Cu/CuO_x and NiFe/Cu/CuO_x

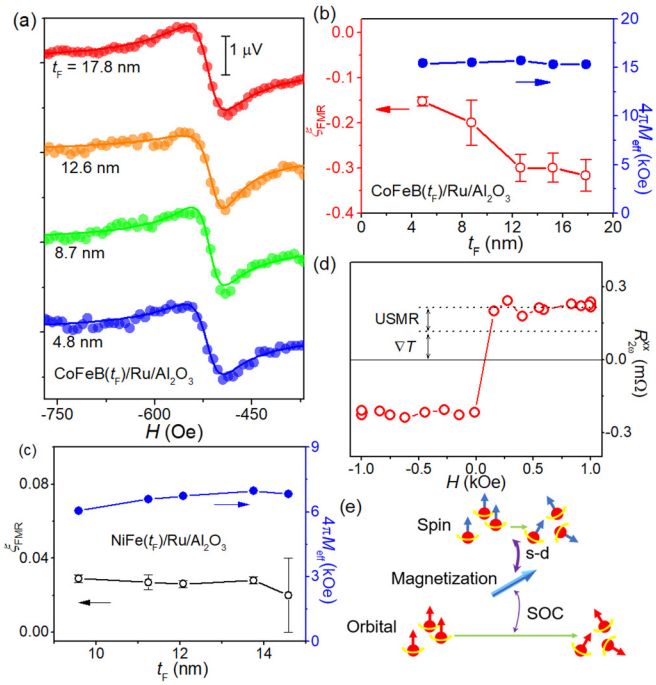

FIG. 2. (a) ST-FMR spectra of CoFeB(t)/Ru(6)/Al_2O_3(2) devices with different CoFeB thicknesses. (b) Ferromagnetic thickness dependence of ξ_{FMR} and $4\pi M_{eff}$ of CoFeB(t_F)/Ru(6)/Al_2O_3(2). (c) ξ_{FMR} and $4\pi M_{eff}$ of NiFe(t_F)/Ru(6)/Al_2O_3(2) as a function of ferromagnetic layer thickness. (d) USMR signal of CoFeB(12.2)/Ru(6)/Al_2O_3(2) at current density 1.7×10^6 A cm^{-2}. ΔT represents the thermal contribution to the second harmonic signal. (e) Schematic of the angular momentum current-to-spin torque conversion processes of OT and spin-orbit torque in the ferromagnetic metal.

in an experimental study [12], although the first-principles calculation gives a positive-sign η_{L-S} for single crystalline Fe, Co, and Ni, which can also explain some OT experiments [11,13]. Likely, these conflicting assertions reflect that the orbital-to-spin conversion could be critically determined by material conditions, such as single or polycrystalline states of FMs, or pure or alloy states of FMs.

The thickness of FM could be a factor for ξ_{FMR}, considering that the orbital-to-spin conversion occurs in the FM layer. The ST-FMR spectra of the CoFeB(t)/Ru(6)/Al_2O_3(2) stack with various CoFeB film thicknesses ($t_F = 4.8$–17.8 nm) is presented in Fig. 2(a). Concomitant ξ_{FMR} and $4\pi M_{eff}$ are summarized in Fig. 2(b). The comparable M_{eff} reflects similar magnetic properties for the CoFeB layer in all of the samples. Note that $|\xi_{FMR}|$ increases with the increase of the CoFeB layer thickness, and finally reaches a saturation value ~0.3 at $t_F = 12.6$ nm. Meawhile, the contribution of the field-like torque could lead to the overestimation of ξ_{FMR} [20]. We never find a sign change of the A component in the CoFeB(t_F)/Ru(6)/Al_2O_3(2) stack, consistent with the sign of the Oersted field torque. [Fig. 2(a)]. The studied CoFeB thickness range is much larger than the typical FM layer thickness, where a field-like torque-induced artifact is important (e.g., $t_F \sim 3$ nm for Pt/CoFe [20]). Hence, the large ξ_{FMR} in the thick FM layer reflects the high torque efficiency. Identical experiments were carried out in NiFe(t)/Ru(6)/Al_2O_3(2) control samples, yielding ξ_{FMR} and $4\pi M_{eff}$ [Fig. 2(c)]. The torque efficiency keeps a value of ξ_{FMR} as small as ~0.03 for all NiFe thicknesses.

We carried out the USMR measurement for the CoFeB(12.2)/Ru(6)/Al_2O_3(2) stack with a thick CoFeB layer [Fig. 2(d)]. Actually, the second harmonic longitudinal resistance signal Rxx 2ω can be generated by both the USMR and thermal effects. We carefully consider the thermal contribution and eventually obtain a pure USMR signal $\Delta R_{USMR}/R = 1.1 \times 10^{-5}$ at a current density of 1.7×10^6 A cm^{-2}, which is larger than the USMR signal in Pt/Co [25], Ta/Co [25], and NiFe/oxidized Cu [26]. This large USMR can be understood owing to the huge orbital torque effect shown in Fig. 2(b) [18].

Depending on the selection of FM materials (CoFeB and NiFe with different values of $\eta_{L\text{-}S}$), OT magnitude and OT dependency on the FM thickness completely change, revealing the unique feature of OT. In conventional spin-orbit torque [27] and other interfacial torque mechanisms, such as anomalous spin-orbit torque [28,29], the torque efficiency is constant with the change in FM thickness. The different FM thickness dependence between OT and other torques can be understood by the different role of FM as an aspect of torque generation [Fig. 2(e)]. For the former, the angular momentum transfer between the orbital current and the magnetization is mediated by SOC. In contrast, for the latter, the angular momentum transfer between the spin current and the magnetization is based on the s-d exchange interaction. Since SOC is much smaller than the s-d exchange interaction, the orbital current can propagate a long distance in FM [15]. Note that a recent Rashba-Edelstein magnetoresistance experiment reported similar ferromagnet thickness-dependent behavior due to the characteristic orbital transport [30]. In comparison, spin-current dephasing occurs rapidly in FM due to the strong s-d exchange interaction, thus the propagation length is much shorter. Such a long propagation length allows the OT to manipulate thick ferromagnet, which is favorable for the memories and magnetic sensor applications.

We now turn toward Ru thickness-dependent orbital torque. CoFeB is fixed to 7 nm for this experiment. Figure 3(a) shows evaluated ξ_{FMR} as a function of Ru thickness in the CoFeB(7)/Ru(t)/Al_2O_3(2) stack. Remarkably, the absolute value of ξ_{FMR} turns out small ($|\xi_{FMR}| = 0.05$) for $t_{Ru} = 2$ nm, but it enhances with increasing Ru thickness. When $t_{Ru} = 7$ nm, $|\xi_{FMR}|$ reaches a maximum of 0.18; a further increase in t_{Ru} makes $|\xi_{FMR}|$ decrease. Measurements of the Ru thickness dependence of OT is performed for the NiFe(7)/Pt(1)/Ru(t_{Ru})/Al_2O_3(2) and NiFe(7)/Ru(t_{Ru})/Al_2O_3(2) stacks [Fig. 3(b)]. Similar to OT in the stack with FM = CoFeB, ξ_{FMR} increases with increasing t_{Ru} for $t_{Ru} < 6$ nm, and decreases when $t_{Ru} > 7$ nm in the NiFe(7)/Pt(1)/Ru(t_{Ru})/Al_2O_3(2) stack. The decreasing $|\xi_{FMR}|$ suggests that an orbital relaxation process reduces OT in the thick Ru layer, which is distinct from OT purely coming from the bulk [11,13]. Hence, the ORE from the Ru/Al_2O_3 interface contributes importantly to the observed large torque effect in the CoFeB/Ru/Al_2O_3 stack. The much smaller torque effect at small t_{Ru} demonstrates that the ORE contribution is also smaller with an ultrathin Ru layer, which

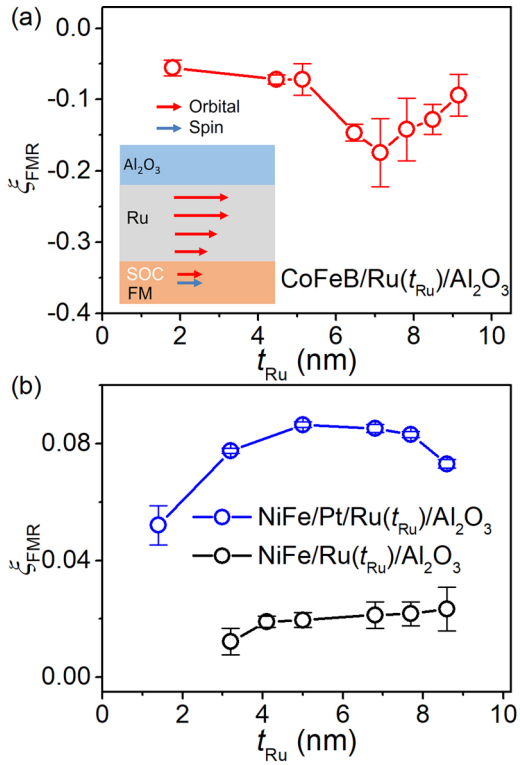

FIG. 3. t_{Ru} Dependence of the calculated ξ_{FMR} of $CoFeB(7)/Ru(t_{Ru})/Al_2O_3(2)$ (a), and $NiFe(7)/Ru(t_{Ru})/Al_2O_3(2)$ (black circles) and $NiFe(7)/Pt(1)/Ru(t_{Ru})/Al_2O_3(2)$ (blue circles) (b). The inset of (a) is the schematic illustration of the orbital current propagating across the Ru layer, converted to the torque via SOC.

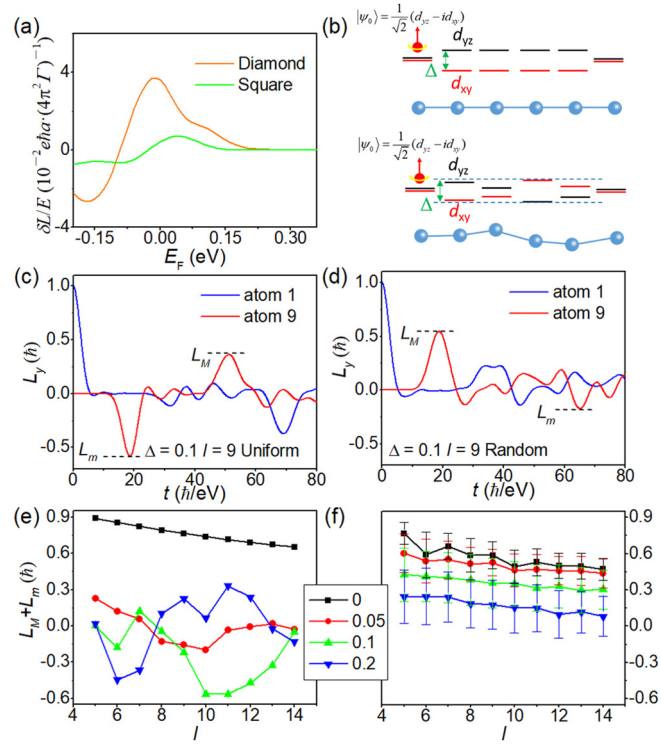

FIG. 4. (a) Fermi-level dependence of the ORE. (b) Schematics of 1D atom chain with uniform crystal field and random crystal field in bulk. The crystal fields of the first and the last atom are set to be zero. (c) and (d) are the time evolution of the orbital angular momentum L_y in the uniform and random crystal field atom chains, respectively. The blue curve represents L_y at the first atom (atom 1), and the red curve represents the L_y at the last atom (atom 9), with crystal field $V = 0.1$ eV and atom number $l = 9$. The positive and negative maximum L_y are labeled as L_M and L_m, respectively. (e) and (f) are the atom number l dependence of $L_M + L_m$ with uniform and random crystal field, respectively, and crystal field magnitude $V = 0$ eV (black), 0.05 eV (red), 0.1 eV (green), and 0.2 eV (blue). Data points for the random crystal field are obtained from 200 simulations, and the error bar is the corresponding standard deviation.

can be ascribed to the degradation of material quality (e.g., roughness, crystalline quality) of the Ru/Al_2O_3 interface [5]. In contrast to the previous results, ξ_{FMR} exhibits no obvious t_{Ru} dependence in the $NiFe(7)/Ru(t_{Ru})/Al_2O_3(2)$ stack. Almost constant ξ_{FMR} for this stack is consistent with the small η_{L-S} of NiFe. We note that, unfortunately, we could not obtain a clear ST-FMR signal for samples with a thick Ru thickness due to the small anisotropic magnetoresistance of CoFeB and the current-shunting effect in the Ru layer. The orbital Hall effect in Ru [31] may also contribute to the torque effect, but cannot explain the decreasing OT efficiency in the thick Ru regime, and thus cannot be the origin of the thickness-dependent behavior. Using other kinds of ferromagnets with both large SOC and anisotropic magnetoresistance for thicker Ru may help to quantify the contributions of ORE and orbital Hall effect further, but is beyond the scope of the present work.

III. THEORY

We theoretically consider orbital generation and transport in the Ru/Al_2O_3 polycrystalline structure. The generation of the orbital current due to ORE requires interfacial orbital hybridization, which can survive in polycrystalline interfaces, as evidenced by the orbital reconstruction-induced voltage control magnetic anisotropy effect in polycrystalline stacks [32,33]. Hence, we develop two tight-binding models on the simple square and diamond lattices, typical two-dimensional lattices; we consider Ru d_{xz}, d_{xy}, and d_{yz} orbitals and O p_x, p_y orbitals [16]. The d orbitals distribute between -0.1 and 0.2 eV [18]. The strength of the ORE can be evaluated by $\delta L/E$, where δL is the nonequilibrium orbital accumulation and E is the applied electric field. As illustrated in Fig. 4(a), ORE in the square and diamond lattice show the same sign and similar Fermi-level dependence. When the d-bands are filled ($E_F > 0.3$ eV), $\delta L/E$ is almost zero. $\delta L/E$ starts to increase when E_F moves toward the middle point of the d-bands and reaches a maximum near $E_F = 0$. When E_F further decreases, $\delta L/E$ starts to drop. Fermi-level dependence reveals that partially filled d-electrons are critical for orbital generation, while the crystal orientation just provides a negligible effect. Notably, the chiral orbital texture depends only on the energy difference between the Ru $d-$ and the O $2p-$states. It would not be influenced by the crystal orientation, causing the survival of the ORE in the polycrystalline samples.

The ORE at the polycrystalline Ru/Al_2O_3 interface corresponds to an average of several single crystals with different orientations. The propagation of orbital current in polycrys-

talline structures is greatly different from that of single crystalline structures. Single crystalline structures with orbital degeneracy provide a long lifetime for the orbital superposition state [15]. However, a crystal field-splitting Δ of the orbitals in the single crystalline structures drives the orbital superposition states into oscillation. It causes a relaxation in the orbital current during the time of $t_1 \sim \hbar/\Delta$. On the other hand, in polycrystalline samples, if the crystal field Δ is random, the electrons carrying the orbital angular momentum could meet both positive and negative oscillation, which cancels out. This cancellation leads to a counterintuitive result; with the same crystal field Δ, polycrystalline structures are more favorable for orbital transport than single crystalline structures.

We now use the quantum evolution equation $|\psi(t+\delta t)\rangle = \exp(-i\frac{\hat{H}}{\hbar}\delta t)|\psi(t)\rangle$ on a one-dimensional (1D) atom chain to calculate the orbital transport in single crystalline and polycrystalline structures. In the initial ($t = 0$) state, the first atom has an electron, and all other orbitals are empty. The electron on the first atom has a wave function $|\psi_0\rangle = \frac{1}{\sqrt{2}}(d_{yz} - id_{xy})$, which gives an orbital angular momentum in y-direction $L_y = \hbar$. The Hamiltonian consists of the crystal field $\pm\Delta$, which is uniform [Fig. 4(b), upper panel] or random [Fig. 4(b), lower panel], with a hopping term J between the same orbital and J' between different orbitals of nearest atoms. We use $J = 0.3$ eV, and J' distributed from –0.06 to 0.06 eV determined by atom orientations, and the detail of the Hamiltonian is given in Ref. [18]. Note that the model for the random crystal field is suitable for polycrystalline structures with small grain size. Considering that the grain size of the Ru layer is less than 10 nm, as supported by the absence of a clear grain in the high-resolution transmission electron microscope observation [18], the condition of the stacks in this study is well fitted with the model.

Figure 4(c) displays the time evolution of the orbital angular momentum at the first and last atoms in an $l = 9$, 1D atom chain with uniform crystal field $\Delta = 0.1$ eV. At $t = 0$, atom 1 has $L_y = \hbar$ and atom 9 has $L_y = 0$. Then, L_y of atom 1 decreases due to electron hopping, and the orbital angular momentum is transferred to the atoms in the middle. When $t = 20\,\hbar/\text{eV}$, the electron wave function reaches atom 9, carrying the orbital angular momentum $-0.6\hbar$. The negative sign reveals that crystal field-induced orbital oscillation accumulates during transport, and orbital angular momentum is switched from the initial state. In contrast, under a random crystal field, the L_y peak value is $0.6\,\hbar$ at $t \sim 20\,\hbar/\text{eV}$, with the same sign as the initial orbital angular momentum due to the compensation of the different oscillation directions at different atoms. To analyze orbital transport efficiency, we evaluate the positive and negative maximum L_y on the last atom, labeled L_M and L_m, respectively, from $t = 0$ to $t = 80\,\hbar/\text{eV}$. Usually, one of L_M and L_m is the L_y peak due to orbital transport, and the other one represents the amplitude of the random orbital fluctuation. Hence $(L_\text{M} + L_\text{m})$ is selected as the figure of merit of orbital transport. We numerically calculate atom chains with atom number $l = 5$ to 15 and $\Delta = 0$, 0.05, 0.1 and 0.2 eV. For the calculation of the random crystal field condition, data points are collected from an average of 200 simulations. As shown in Fig. 4(e), the strongest orbital transport is shown for $\Delta = 0$ with a uniform crystal field. In the uniform crystal field condition, the positive-negative-positive orbital oscillation starts to be driven when $\Delta = 0.05$ eV, and similar behavior persists for $\Delta > 0.05$ eV.

At $\Delta = 0$, due to orbital mixing hopping J', orbital transport is less efficient when the crystal field is random [Fig. 4(f)]. However, as Δ increases, orbital transport is maintained without oscillation, although decay of orbital angular moment is not negligible. Hence, we conclude that long-range orbital transport can occur in the random crystal field case if the crystal field is smaller than the hopping energy. In contrast, a uniform crystal field with the same magnitude can quickly destroy orbital transport. Although band dispersion and filling in actual samples can lead to more complicated crystal field dependence of orbital transport [14], the 1D model captures the key point of the different orbital oscillation behavior between uniform and random crystal fields, which should appear in the actual samples in complex condition. Thus, this model indicates that polycrystalline structures are possibly more efficient for some materials with crystal fields than single crystalline structures.

The principle of material selection for orbital sources in OT devices can be summarized accordingly. Compared with single crystals, polycrystalline stacks are much more compatible with silicon-based technology and provide an opportunity for long-range orbital transport in the presence of a crystal field. In polycrystalline stacks, orbital generation requires d-states near the Fermi energy for orbital hybridization. Orbital transport is affected by a number of factors, such as crystal field, orbital-mixing hopping, and disorder-induced localization. Hence, the orbital source should be selected from materials with relatively simple structures and itinerant d-electrons. Besides Ru presented here, efficient orbital generation and transport could be explored in other transition metals and simple conductive transition metal oxides with itinerant d-electrons, such as IrO_2 [34].

IV. CONCLUSION

In conclusion, we have demonstrated remarkable OT in the polycrystalline FM/Ru/Al_2O_3 stack, mediated by efficient long-range orbital transport in the uniform polycrystalline Ru layer. We find characteristic behaviors of OT: (i) the sign and magnitude of the torque efficiency are strongly dependent on the FM materials and insertion layers according to the sign and magnitude of their SOC; and (ii) torque efficiency is enhanced with increasing CoFeB layer thickness t_F, with a large saturation torque efficiency 0.3 for $t_\text{F} = 12$ nm, consistent with the long propagation length of the orbital current in the ferromagnet. The torque efficiency reaches a maximum value at a Ru layer thickness of 7 nm, and decreases with Ru layer thickness, revealing the ORE at the Ru/Al_2O_3 interface as the origin of the orbital current. The tight-binding model with different crystal structures shows that ORE can be maintained at polycrystalline interfaces. Our quantum evolution simulation shows the unique random processing feature of orbital transport in polycrystalline materials, which enables long-range orbital transport in polycrystalline samples even in the presence of a crystal field. Our results show that transition

metal-based materials with a small SOC, simple structure, and itinerant d-electrons can provide a suitable platform for studying orbital transport in polycrystalline structures and developing torque devices.

Note added. Recently, a preprint reported the long-range orbital transport in Ti/Ni and W/Ni bilayers [40]. In that work, the orbital current is generated from the bulk orbital Hall effect, while our work focuses on the orbital current generated from the interfacial orbital Rashba effect.

ACKNOWLEDGMENTS

The authors acknowledge financial support from the National Key Research and Development Program of China (MOST) (Grant No. 2021YFB3601301), the National Natural Science Foundation of China (Grant No. 51871130), and the Natural Science Foundation of Beijing, China (Grant No. JQ20010). C.S. is grateful to the support of ICFC, Tsinghua University. J.K. appreciates the financial support from JSPS KAKENHI (Grant No. 19K05258).

[1] L. Liu, C.-F. Pai, Y. Li, H. W. Tseng, D. C. Ralph, and R. A. Buhrman, Science **336**, 555 (2012).
[2] C. Song, R. Zhang, L. Liao, Y. Zhou, X. Zhou, R. Chen, Y. You, X. Chen, and F. Pan, Prog. Mater. Sci. **118**, 100761 (2021).
[3] I. M. Miron, K. Garello, G. Gaudin, P.-J. Zermatten, M. V. Costache, S. Auffret, S. Bandiera, B. Rodmacq, A. Schuhl, and P. Gambardella, Nature (London) **476**, 189 (2011).
[4] X. Chen, Y. Liu, G. Yang, H. Shi, C. Hu, M. Li, and H. Zeng, Nat. Commun. **9**, 2569 (2018).
[5] J. Kim, D. Go, H. Tsai, D. Jo, K. Kondou, H.-W. Lee, and Y. C. Otani, Phys. Rev. B **103**, L020407 (2021).
[6] S. Ding, A. Ross, D. Go, L. Baldrati, Z. Ren, F. Freimuth, S. Becker, F. Kammerbauer, J. Yang, G. Jakob, Y. Mokrousov, M. Klaui, Phys. Rev. Lett. **125**, 177201 (2020).
[7] D. Go, D. Jo, C. Kim, and H. W. Lee, Phys. Rev. Lett. **121**, 086602 (2018).
[8] D. Go and H.-W. Lee, Phys. Rev. Res. **2**, 013177 (2020).
[9] H. Kontani, T. Tanaka, D. S. Hirashima, K. Yamada, and J. Inoue, Phys. Rev. Lett. **102**, 016601 (2009).
[10] D. Jo, D. Go, and H.-W. Lee, Phys. Rev. B **98**, 214405 (2018).
[11] S. Lee, M.-G. Kang, D. Go, D. Kim, J.-H. Kang, T. Lee, G.-H. Lee, N. J. Lee, S. Kim, K.-J. Kim, and B.-G. Park, Commun. Phys. **4**, 234 (2021).
[12] Y. Tazaki, Y. Kageyama, H. Hayashi, T. Harumoto, T. Gao, J. Shi, and K. Ando, arXiv:2004.09165.
[13] D. Lee, D. Go, H.-J. Park, W. Jeong, H.-W. Ko, D. Yun, D. Jo, S. Lee, G. Go, J. H. Oh, K. J. Kim, B.-G. Park, B.-C. Min, H. C. Koo, H.-W. Lee, O. Lee, and K.-J. Lee, Nat. Commun. **12**, 6710 (2021).
[14] H. An, Y. Kageyama, Y. Kanno, N. Enishi, and K. Ando, Nat. Commun. **7**, 13069 (2016).
[15] D. Go, D. Jo, K.-W. Kim, S. Lee, M.-G. Kang, B. G. Park, S. Blügel, H. W. Lee, and Y. Mokrousov, arXiv:2106.07928.
[16] D. Go, D. Jo, T. Gao, K. Ando, S. Blügel, H.-W. Lee, and Y. Mokrousov, Phys. Rev. B **103**, L121113 (2021).
[17] Z. Wen, J. Kim, H. Sukegawa, M. Hayashi, and S. Mitani, AIP Adv. **6**, 056307 (2016).
[18] See Supplemental Material at http://link.aps.org/supplemental/10.1103/PhysRevB.105.104434 for details of the sample preparation, spin pumping, material characterization, ST-FMR spectra, USMR measurement, and theoratical assertion, which includes Refs. [5,15,19,25,26,35–39].
[19] L. Liu, T. Moriyama, D. C. Ralph, and R. A. Buhrman, Phys. Rev. Lett. **106**, 036601 (2011).
[20] C.-F. Pai, Y. Ou, L. H. Vilela-Leão, D. C. Ralph, and R. A. Buhrman, Phys. Rev. B **92**, 064426 (2015).
[21] W. Zhang, W. Han, X. Jiang, S.-H. Yang, and S. S. P. Parkin, Nat. Phys. **11**, 496 (2015).
[22] H. Wu, S. A. Razavi, Q. Shao, X. Li, K. L. Wong, Y. Liu, G. Yin, and K. L. Wang, Phys. Rev. B **99**, 184403 (2019).
[23] Y. Omori, E. Sagasta, Y. Niimi, M. Gradhand, L. E. Hueso, F. Casanova, and Y. C. Otani, Phys. Rev. B **99**, 014403 (2019).
[24] R. Bonin, M. L. Schneider, T. J. Silva, and J. P. Nibarger, J. Appl. Phys. **98**, 123904 (2005).
[25] C. O. Avci, K. Garello, A. Ghosh, M. Gabureac, S. F. Alvarado, and P. Gambardella, Nat. Phys. **11**, 570 (2015).
[26] G. Okano, M. Matsuo, Y. Ohnuma, S. Maekawa, and Y. Nozaki, Phys. Rev. Lett. **122**, 217701 (2019).
[27] J. Kim, J. Sinha, M. Hayashi, M. Yamanouchi, S. Fukami, T. Suzuki, S. Mitani, and H. Ohno, Nat. Mater. **12**, 240 (2013).
[28] J. D. Gibbons, D. MacNeill, R. A. Buhrman, and D. C. Ralph, Phys. Rev. Appl. **9**, 064033 (2018).
[29] Z. Luo, Q. Zhang, Y. Xu, Y. Yang, X. Zhang, and Y. Wu, Phys. Rev. Appl. **11**, 064021 (2019).
[30] S. Ding, Z. Liang, D. Go, C. Yun, M. Xue, Z. Liu, S. Becker, W. Yang, H. Du, C. Wang, Y. Yang, G. Jakob, M. Klaui, Y. Mokrousov, and J. Yang, Phys. Rev. Lett. **128**, 067201 (2022).
[31] D. Go, D. Jo, H.-W. Lee, M. Kläui, and Y. Mokrousov, EPL **135**, 37001 (2021).
[32] T. Nozaki, Y. Shiota, M. Shiraishi, T. Shinjo, and Y. Suzuki, Appl. Phys. Lett. **96**, 022506 (2010).
[33] W. G. Wang, M. Li, S. Hageman, and C. L. Chien, Nat. Mater. **11**, 64 (2011).
[34] K. Fujiwara, Y. Fukuma, J. Matsuno, H. Idzuchi, Y. Niimi, Y. Otani, and H. Takagi, Nat. Commun. **4**, 2893 (2013).
[35] S. Emori, T. X. Nan, A. M. Belkessam, X. J. Wang, A. D. Matyushov, C. J. Babroski, Y. Gao, H. Lin, and N. X. Sun, Phys. Rev. B **93**, 180402(R) (2016).
[36] G. Y. Guo, S. Maekawa, and N. Nagaosa, Phys. Rev. Lett. **102**, 036401 (2009).
[37] C.-F. Pai, L. Liu, Y. Li, H. W. Tseng, D. C. Ralph, and R. A. Buhrman, Appl. Phys. Lett. **101**, 122404 (2012).
[38] D. C. Mahendra, R. Grassi, J.-Y. Chen, M. Jamali, D. R. Hickey, D. Zhang, Z. Zhao, H. Li, P. Quarterman, Y. Lv, M. Li, A. Manchon, K. A. Mkhoyan, T. Low, and J.-P. Wang, Nat. Mater. **17**, 800 (2018).
[39] H. Wu, P. Zhang, P. Deng, Q. Lan, Q. Pan, S. A. Razavi, X. Che, L. Huang, B. Dai, K. Wong, X. Han, K. L. Wang, Phys. Rev. Lett. **123**, 207205 (2019).
[40] H. Hayashi, D. Jo, D. Go, Y. Mokrousov, H.-W. Lee, and K. Ando, arXiv:2202.13896 [cond-mat.mes-hall].